



Monopole and quadrupole capillary interaction in turbulent interfacial suspensions

Seunghwan Shin ond Filippo Coletti on

¹Department of Mechanical and Process Engineering, ETH Zurich, 8092 Zurich, Switzerland **Corresponding author:** Seunghwan Shin, seshin@ethz.ch

(Received 29 July 2025; revised 13 September 2025; accepted 15 September 2025)

Particle suspensions at the interface of turbulent liquids are governed by the balance of capillary attraction, strain-induced drag and lubrication. Here, we extend previous findings, obtained for small particles whose capillary interactions are dominated by quadrupolar-mode deformation of the interface, to larger spherical and disc-shaped particles experiencing monopole-dominant capillarity. By combining pair-approach experiments, two-dimensional turbulent flow realizations and particle imaging, we demonstrate that particles experiencing monopole-dominant attraction exhibit enhanced clustering compared with their quadrupole-dominant counterparts. We introduce an interaction scale defined by balancing viscous drag and capillary attraction, which is compared with the particle size and interparticle distance. This allows us to map the clustering behaviour onto a parameter space solely defined by those characteristic length scales. This yields a unified framework able to predict the tendency to cluster (and the concentration threshold for those clusters to percolate) in a vast array of fluid—particle systems.

Key words: particle/fluid flows, suspensions

1. Introduction

Dense turbulent suspensions at fluid interfaces are commonly encountered in a variety of natural and industrial settings, from microplastics on the ocean surface to mineral processing by froth flotation. Yet, understanding their behaviour remains a formidable challenge. These systems involve an intricate interplay of turbulence, interfacial tension and multi-particle interactions across a wide range of scales, defying simple predictive models. Historically, research on particle-laden flows has focused either on dense suspensions dominated by viscous forces and short-range interactions (Wagner & Brady 2009; Brown & Jaeger 2014; Denn & Morris 2014) or dilute suspensions of inertial

particles in turbulence (Toschi & Bodenschatz 2009; Balachandar & Eaton 2010; Monchaux, Bourgoin & Cartellier 2012; Brandt & Coletti 2022). Bridging those extremes, however, has proven challenging, as experiments and simulations become increasingly complex when both high concentration and turbulence coexist (Matas, Morris & Guazzelli 2003; Picano, Breugem & Brandt 2015; Baker & Coletti 2019; Hogendoorn *et al.* 2023).

Particles at fluid interfaces introduce additional complexities, which have been studied extensively both for non-Brownian (Singh & Joseph 2005; Madivala, Fransaer & Vermant 2009) and colloidal suspensions (Fuller & Vermant 2012; Garbin 2019). In this case, the collective behaviour is driven by fundamentally different mechanisms: while dense suspensions cluster due to hydrodynamic interactions (Guazzelli, Morris & Pic 2011) and turbulent suspensions do because of particle/fluid inertia (Brandt & Coletti 2022), in interfacial suspensions, agglomeration is driven by capillarity (Protière 2023). Reaching a predictive understanding of dense turbulent interfacial suspensions is a formidable challenge because of the coexistence of such mechanisms.

In systems comprising a large number of particles, an especially relevant aspect is the tendency to percolate, i.e. to form connected networks spanning the entire domain (Stauffer & Aharony 2018). In dense particle suspensions, percolating networks of contacts (lubricated or direct) among particles typically emerge at a concentration threshold close to but below the jamming limit (Morris 2020). Percolating clusters are critical for the rheological and transport properties, occurring for particles of different nature, size, shape and deformability; for recent examples, see Möbius *et al.* (2021), Alicke, Stricker & Vermant (2023), van der Naald *et al.* (2024), Girotto *et al.* (2024), Marin & Souzy (2024), Kim & Hilgenfeldt (2024). The tendency of the system to percolate is usually assessed as a function of concentration and applied stress. While the protocols vary across the various settings, the applied stress commonly comes from geometrically simple compressive/extensive strain or pressure-driven flow of the carrier phase. In dense turbulent suspensions, though, the main source of stress may be the fluid fluctuating energy; this is the case in the present study.

We recently reported on the behaviour of dense turbulent suspensions at the interface of turbulent liquids (Shin & Coletti 2024; Vowinckel 2024; Shin, Stricker & Coletti 2025). These were experimentally realised in electromagnetically driven fluids laden with millimetric spherical particles, over broad ranges of concentration, interfacial tension and turbulence intensity. We investigated the competing role of viscous drag, capillary attraction and lubrication, and demonstrated how their balance determines the transition between different regimes in terms of particle energy, diffusivity, clustering properties and tendency to percolate.

Previously (Shin & Coletti 2024; Shin *et al.* 2025), we used particles less than 2 mm in diameter and with density close to that of the carrier fluid. For those, buoyancy does not appreciably deform the liquid interface and the capillary inter-particle attraction is dominated by the short-range quadrupolar mode of interfacial distortion (Stamou, Duschl & Johannsmann 2000; Botto *et al.* 2012; Liu, Sharifi-Mood & Stebe 2018). In many practical situations, larger particle size and/or density mismatch induce significant interfacial deformation, and the capillary interaction is dominated by the monopole mode that decays much slower (roughly logarithmically; see Vella & Mahadevan 2005). We ask the following questions. How does such a longer-range interaction change the clustering behaviours and the percolation threshold? Do dense turbulent interfacial suspensions admit a unified description, encompassing both quadrupolar and monopolar modes of surface deformation?

To address these questions, we consider both spherical and disc-shaped particles and examine the distinct clustering and percolation behaviours. By introducing an effective

Label	Particle type	$\rho_p~({\rm g~cm^{-3}})$	d_p (mm)	Re	Ca	ϕ	Bo	Bo_c
1SL	PE spheres	1.0	1.09	566-1747	0.09-0.29	0.01 - 0.43	0.17	0.46 - 0.66
1DL	PE spheres	1.0	1.09	229 - 1035	0.41 - 1.84	0.14 - 0.44	0.09	0.74 - 1.23
2DL	PE spheres	0.96	1.84	192 - 1047	0.49 - 2.69	0.08 - 0.71	0.27	0.69 - 1.39
4SL	PP spheres	0.9	3.9	491 - 1553	0.31 - 0.98	0.02 - 0.46	2.23	0.65 - 0.98
4DL	PP spheres	0.9	3.9	175 - 819	0.63 - 2.93	0.08 - 0.76	1.19	0.75 - 2.08
10dDL	PP discs	0.9	10 (1 mm-thick)	229-969	0.63 - 2.67	0.04 - 0.70	7.85	0.85 - 1.64

Table 1. Summary of the main experimental parameters investigated in this study, including the Reynolds number Re, the capillary number Ca, the areal fraction ϕ , the Bond number Bo and the interaction Bond number Bo_c , all defined in the text. PE and PP refer to polyethylene and polypropylene, respectively.

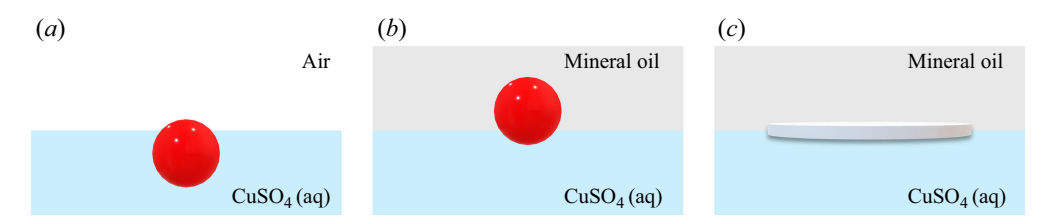


Figure 1. Schematic illustration of the particle–fluid configurations investigated: (a) a sphere in the single-layer (SL) configuration; (b) a sphere in the double-layer (DL) configuration; and (c) a disc in the double-layer (dDL) configuration.

capillary length scale, we reconcile monopolar and quadrupolar regimes into a single predictive framework, enabling quantitative predictions for a wide range of conditions. The remainder of the paper is organised as follows: in § 2, we describe the experimental methodology and the parameter space; in § 3, we present and discuss the results, first in terms of the prevalent mode of capillary attraction and then in terms of clustering and percolation; in § 4, we draw conclusions and discuss the outlook.

2. Experimental methodology

We employ different fluid–particle combinations, as summarised in table 1. Polyethylene spheres with diameters smaller than 2 mm exhibit quadrupole-dominant interactions, as shown by Shin & Coletti (2024). Larger polypropylene spheres and 1 mm-thick polypropylene discs, however, interact prevalently by monopolar capillarity, as we will show. Two fluid-layer configurations are studied. In the single-layer (SL) case, the particles float at the air–water interface of a 7-to-8 mm-deep conductive aqueous solution (10 % CuSO₄ by mass, density $\rho_f = 1.08 \text{ g mL}^{-1}$, kinematic viscosity $\nu = 1.0 \times 10^{-6} \text{ m}^2 \text{ s}^{-1}$). In the double-layer (DL) case, a 2-to-4 mm layer of mineral oil ($\rho_f = 0.84 \text{ g mL}^{-1}$, $\nu = 1.9 \times 10^{-5} \text{ m}^2 \text{ s}^{-1}$) is added on top of the same aqueous phase, and particles primarily reside within the oil layer, partially wetted by the underlying water. The particle/interface configurations are schematically illustrated in figure 1.

The capillary force is obtained by pair-approach experiments. Pairs of identical particles are placed at distance of approximately 10 mm from each other in a tray containing the fluid layer(s). The pairs approach each other due to capillarity, and their positions and trajectories are measured with sub-pixel accuracy using the same imaging equipment and methodology as of Shin & Coletti (2024).

The particle-laden fluid layers are stirred into quasi-two-dimensional (Q2-D) turbulent flows using the apparatus described in detail in earlier studies (Shin, Coletti & Conlin 2023; Shin & Coletti 2024; Shin et al. 2025). This features a $320 \times 320 \text{ mm}^2$ tray above an 8×8 array of cylindrical neodymium-iron-boron magnets. These are arranged in a chequerboard pattern with alternating polarities, which combine with the DC current between copper electrodes at opposite sides of the tray to induce Lorentz forces. The centre-to-centre magnet spacing $L_F = 35 \text{ mm}$ provides the forcing length scale in the turbulent Reynolds number $Re = u_{rms}L_F/\nu$, where u_{rms} is the root-mean-square flow velocity.

The Q2-D flow achieves a fully turbulent character, as extensively characterised by Shin *et al.* (2023, 2025). In particular, the scaling of the third-order longitudinal structure function of the velocity fluctuations transitions from cubic to linear for separations $\sim L_F$. Correspondingly, the energy spectrum displays the expected scaling k^{-3} in the enstrophy-cascade subrange, i.e. for wavenumbers $k > 2\pi/L_F$ (Boffetta & Ecke 2012).

We vary the areal fraction $\phi \equiv N_p(\pi d_p^2/4)/A_{FOV}$ between 1% and 76%, where N_p is the average number of particles in the field of view of area A_{FOV} . The relative strength of the applied stress is quantified by the capillary number Ca: this compares viscous drag imposed by the fluid strain rate (separating particle pairs) and capillary attraction, both evaluated at contact, $Ca \equiv F_{drag,r=d_p}/F_{cap,r=d_p}$.

We explain how the capillary force is evaluated in the following section, while the scaling of the drag force is briefly sketched here (for details, see Shin & Coletti 2024). Assuming a Stokesian formulation, the force F_{drag} pulling two particles apart is linear in the relative velocity between the particles and the surrounding fluid. Considering a pair of adjacent particles aligned with the extensional eigenvector of the local strain rate tensor, the relative velocity of the fluid across the pair is $\Delta u_f \approx \dot{\epsilon}_{max} d_p$, where $\dot{\epsilon}_{max}$ is the maximal principal strain rate. Neglecting the incipient motion of the particles away from each other, Δu_f equals the relative velocity between fluid and particles. The strain rate is estimated as $\dot{\epsilon}_{max} \sim u_{rms}/L_F$, with the numerical prefactor determined by approximating the flow as an array of Taylor–Green vortices. Here, we have assumed that 'strain cells' at the scale of the particles are mainly responsible for breakup of adjacent particles. This assumption is consistent with measurements of the aggregate breakup rate, as discussed by Qi, Shin & Coletti (2025b).

Contact is defined based on a search radius around each centroid of approximately $1.2d_p$, determined from low-Ca snapshots where tightly bound clusters and isolated particles are clearly distinguishable. We define clusters as sets of four or more adjacent particles (the specific minimum number being inconsequential for the final conclusions). We monitor the clustering fraction χ_{cl} (the number of clustered particles normalised by the total number of imaged particles) and the percolation fraction χ_p . The latter is the fraction of images in which a cluster spans the field of view side-to-side. We stress that, via imaging, we can only assess connectivity percolation which is based on contact/adjacency, and not rigidity percolation which requires evaluating inter-particle forces (Sedes $et\ al.\ 2022$).

Moreover, due to the high particle concentration achieved, the fluid velocity is measured in the single-phase experiments. Using the latter in the evaluation of the drag implies the assumption that the fluid forcing is approximately unaffected by the particles. In the dense regimes, the dispersed phase is in fact expected to influence the fluid. However, the agreement between the observations and the regime transitions theorised by Shin & Coletti (2024) suggests that the assumption is, to first order, tenable. Moreover, the pair dispersion measurements by Shin *et al.* (2025) indicate that the energy dissipation rate due to lubrication is responsible for the reduction in particle kinetic energy at high concentration, rather than the clusters damping the fluid flow energy.

3. Results and discussion

We begin by assessing the prevalent mode of capillary attraction through pair-approach experiments. As shown by Shin & Coletti (2024), for the smaller spheres ($d_p = 1.09$ and 1.84 mm), the quadrupolar contribution dominates (Liu *et al.* 2018):

$$F_{cap} = -\frac{3\pi \gamma h_{qp}^2 d_p^4}{r^5},\tag{3.1}$$

where γ is the interfacial tension and h_{qp} is the amplitude of the quadrupolar mode. The latter is related to the particle surface roughness and is estimated by a least-square fit of the centre-to-centre inter-particle separation r as a function of time t:

$$r_0^6 - r^6(t) = \frac{12\gamma h_{qp}^2 d_p^3 t}{\mu},\tag{3.2}$$

where r_0 is the initial separation and μ is the dynamic viscosity of the fluid in which the particles are immersed (Shin & Coletti 2024). Balancing F_{cap} against Stokes drag and lubrication yields the following expression of the relative velocity:

$$v_{rel}(r) = \frac{2\gamma h_{qp}^2 d_p^3 G(x)}{\mu r^5},$$
(3.3)

with dimensionless separation $x = r/d_p$, and $G(x) \approx 1-3/(4x) + 1/(8x^3)-15/(64x^4)-4.46/1000(2x-1.7)^{-2.867}$ the hydrodynamic mobility accounting for reduced relative velocities at small particle separations due to lubrication effects (Batchelor 1976). Here, v_{rel} initially increases as particles move closer and capillarity grows stronger, and subsequently decreases as lubrication forces dominate at small separations. In contrast, the larger particles (3.9 mm spheres and 10 mm discs) exhibit longer-range capillary attractions associated with the monopolar mode of interfacial deformation:

$$F_{cap}(r) = -C_s K_1 \left(\frac{r}{l_c}\right),\tag{3.4}$$

where C_s is a prefactor determined by vertical force balance between buoyancy and interfacial tension, $l_c \equiv \sqrt{\gamma/(\Delta \rho_f g)}$ is the capillary length with $\Delta \rho_f$ the density difference between two fluids, g is the gravitational acceleration, and K_1 is a modified Bessel function of the second kind (Vella & Mahadevan 2005; Dalbe *et al.* 2011). In this case, one obtains a relative velocity:

$$v_{rel}(r) = \frac{2C_s G(x)}{3\pi \mu d_p} K_1 \left(\frac{r}{l_c}\right). \tag{3.5}$$

As the drag is approximately linear (Shin & Coletti 2024), the full capillary-driven interaction force and the associated relative velocity are obtained as the sum of the quadrupolar and monopolar components. As shown in figure 2, the behaviour of the millimetric spheres in case 2DL (as well as in case 1SL, not shown) is dominated by the quadrupolar components at small separations, while the slowly decaying monopolar component takes over at further distances (figure 2a). However, for the larger spheres (as well as the discs, not shown), the monopolar component prevails at all separations (figure 2b). As capillary attraction becomes stronger at small separations, for simplicity, we refer to the two behaviours as quadrupole-dominant and monopole-dominant, respectively.

Having determined the prevalent capillary interaction modes, we now examine the clustering and percolation behaviour for both classes of particles. Figure 3(a,b) show

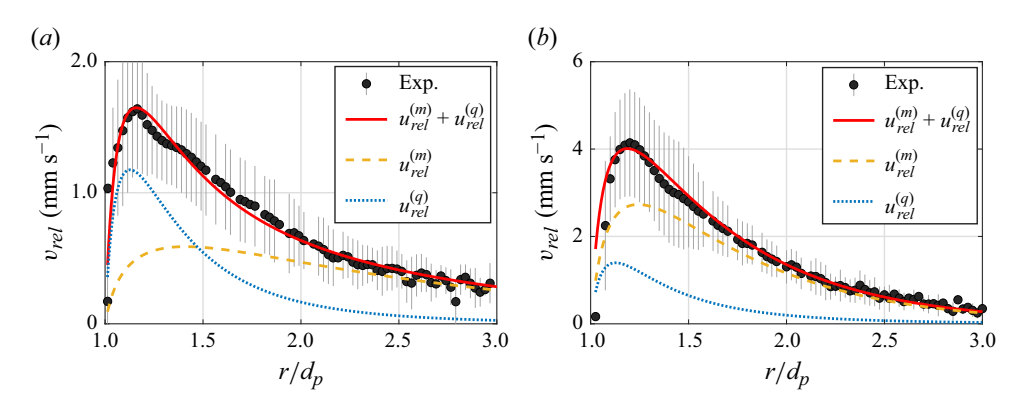


Figure 2. Measured relative velocity $v_{rel}(r)$ compared with theoretical predictions obtained by superposing monopolar and quadrupolar capillary interactions for the (a) 2DL and (b) 4SL, respectively. Error bars represent the standard deviations obtained from five individual experiments.

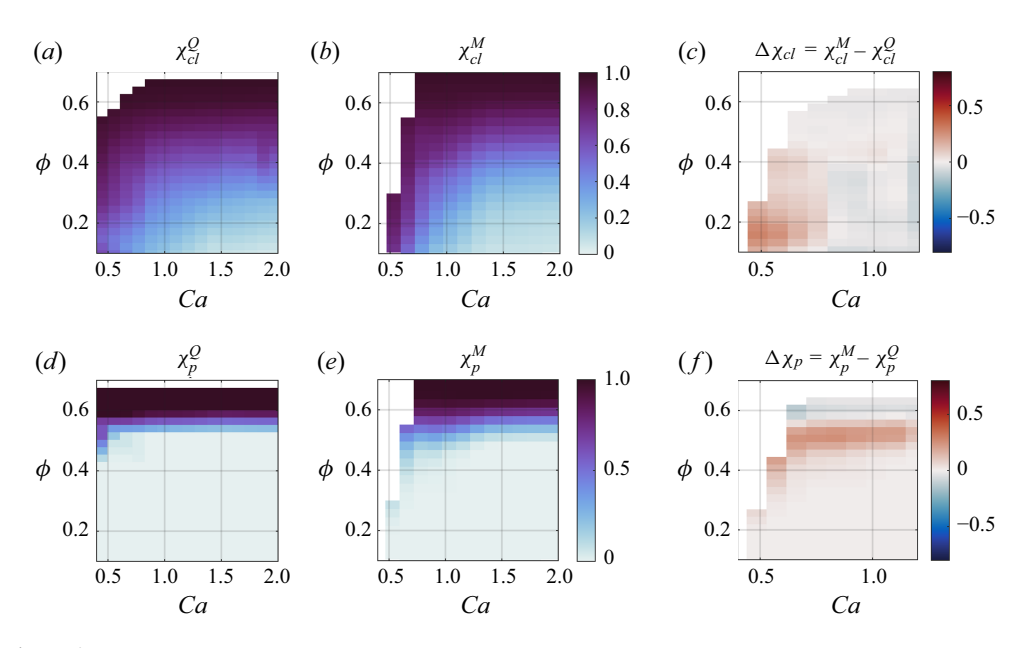


Figure 3. Maps of clustering fraction χ_{cl} for (a) quadrupole-dominant and (b) monopole-dominant cases in the original $Ca-\phi$ parameter space, with (c) the difference $\Delta\chi_{cl}$. Maps of percolation fraction χ_p for (d) quadrupole-dominant and (e) monopole-dominant cases, with (f) the difference $\Delta\chi_p$. Panels (c) and (f) highlight the enhanced clustering and percolation tendencies of the monopole-dominant cases, particularly at Ca < 1.

the clustering fraction χ_{cl} across the explored range of Ca and ϕ for the quadrupole-dominant (1SL, 2DL) and monopole-dominant cases (4SL, 4DL, 10dDL), respectively; figure 3(d,e) present the corresponding percolation fraction χ_p for these two cases. When Ca > 1, both classes exhibit essentially identical behaviour: drag dominates particle dynamics, rendering capillary interactions secondary. When Ca < 1, however, the monopole-dominant cases demonstrate notably stronger clustering and a lower percolation threshold. The difference in these observables between the two cases is quantified by the following metrics:

Journal of Fluid Mechanics

$$\Delta \chi_{cl} = \chi_{cl}^M - \chi_{cl}^Q, \quad \Delta \chi_p = \chi_p^M - \chi_p^Q, \tag{3.6}$$

where the superscripts M and Q denote the monopole-dominant and quadrupole-dominant cases, respectively. Maps of $\Delta \chi_{cl}$ and $\Delta \chi_p$ (figure 3c.f) highlight the enhanced tendency towards clustering and percolation in the monopole-dominant cases at low Ca. This is attributed to the difference in spatial variation between the quadrupolar interaction, decaying as r^{-5} according to (3.1), and the monopolar one, falling off approximately as r^{-1} (since $K_1(r) \approx 1/r$ for $r \to 0$). Thus, even for the same Ca (defined at particle contact), monopolar interactions maintain significant strength at much greater separations.

To rationalise these differences, we introduce an effective interaction length r_c defined as the separation at which the capillary attraction equals the strain-induced drag pulling particles apart, i.e. $F_{cap}(r_c) = F_{drag}(r_c)$. By this definition, particle pairs feel a net attractive force and tend to aggregate for $r < r_c$ and disperse for $r > r_c$. If $r_c < d_p$ (i.e. Ca > 1), drag prevails even at particle contact. For particles experiencing predominantly quadrupolar-mode capillarity, $F_{cap}(r) = F_{cap}(d_p)(d_p/r)^5$. Thus, at the separation r^Q such that $F_{cap}(r_c^Q) = F_{drag}(r_c^Q)$, we have

$$F_{cap}(r) = F_{cap}(d_p) \left(\frac{d_p}{r_c^Q}\right)^5, \tag{3.7}$$

which yields

$$\frac{r_c^Q}{d_p} = Ca^{-1/6}. (3.8)$$

For monopole-dominant particles, however, the spatial dependency of the capillary attraction involves the modified Bessel function, leading to

$$\frac{r_c^M}{d_p} = \frac{1}{Ca} \frac{K_1(r_c^M/l_c)}{K_1(d_p/l_c)}.$$
(3.9)

As this relation involves the modified Bessel function K_1 , it cannot be inverted analytically, and thus r_c^M/d_p must be computed numerically. Moreover, unlike r_c^Q/d_p , the monopolar interaction length scale explicitly depends on the fluid–fluid interface through the capillary length l_c . This is illustrated in figure 4(a), plotting the dimensionless interaction length r_c/d_p as functions of Ca. The monopole-dominant cases, which are configuration-dependent, exhibit larger interaction lengths especially at low Ca. At Ca > 1, all cases yield $r_c < d_p$ by definition: clusters tend to break up regardless of the dominant capillary attraction mode, consistent with the observations made in figure 3.

To unify monopolar- and quadrupolar-dominant behaviours, we define an 'interaction Bond number':

$$Bo_c \equiv \left(\frac{d_p}{r_c}\right)^2. \tag{3.10}$$

In analogy with the classical Bond number $Bo = (d_p/l_c)^2$ (also listed in table 1), Bo_c compares the particle size with the dynamically relevant length scale, though it quantifies the balance between drag and capillary attraction rather than between gravity and surface tension. From (3.8), for the quadrupolar-dominant cases,

$$Bo_c^Q = Ca^{1/3},$$
 (3.11)

whereas the monopolar-dominant cases require numerical evaluation of Bo_c^M . Figure 4(b,c) display χ_{cl} and χ_p in the $Bo_c-\phi$ space: the smooth and monotonic behaviour

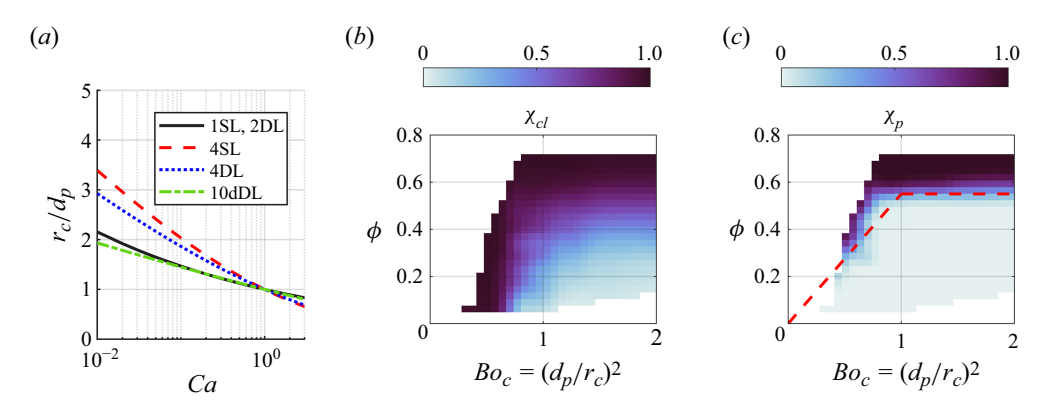


Figure 4. (a) Dimensionless effective capillary interaction length r_c/d_p as a function of the capillary number Ca for quadrupolar (3.8) and monopolar (3.9) cases. (b) Clustering fraction χ_{cl} and (c) percolation fraction χ_p for both quadrupole- and monopole-dominant cases presented in the unified $Bo_c-\phi$ parameter space. The red dashed line indicates the theoretical percolation threshold (3.13).

indicates that this pair of parameters captures the unified behaviour of both monopolar and quadrupolar classes.

We remark that, because an explicit analytical relation between Ca and Bo_c is not available for the monopolar case, the $Bo_c-\phi$ space cannot be obtained by a simple mapping from the $Ca-\phi$ space. Therefore, the definition of Bo_c is necessary to unify the monopolar and quadrupolar cases. Moreover, introducing the interaction length allows a concise rationalisation of the problem: because the areal fraction is determined by the particle diameter and the interparticle distance, $\phi = \pi d_p^2/(4r_{int}^2)$, the entire parameter space is expressed in terms of the three defining scales of the system: d_p , r_c and r_{int} .

Unlike Bo_c , however, Ca can be directly evaluated from the input parameters, and therefore the $Ca-\phi$ representation introduced by Shin & Coletti (2024) remains advantageous to describe the main regimes characterising the system.

As shown by Shin *et al.* (2025), percolation at Ca > 1 is governed by geometric constraints: it occurs for areal fractions above a constant value $\phi_0 \sim 0.55$, approximately equal to the saturation limit of a synthetic set of particles generated by random sequential adsorption (RSA, see Evans 1993).

This approach virtually distributes non-overlapping circles, neglecting any forcing length scale and inter-particle interactions except for the excluded volume. Shin *et al.* (2025) indeed showed how, in the high-Ca limit, the cluster statistics match those of RSA-generated configurations. This reinforces the interpretation that sufficiently strong turbulent forcing enforces stochastic configurations, in which case, the onset of percolation is controlled by excluded-volume effects rather than by cohesive interactions. In contrast, at Ca < 1, enhanced capillary attraction leads to the formation of fractal-like clusters which trigger percolation at lower areal fractions, with a threshold ϕ_c dependent on Ca. Despite this observation, no explicit predictive framework was provided by Shin *et al.* (2025) to account for the reduced percolation threshold in the capillary-dominated regime. However, the concept of interaction length naturally leads to a quantitative unified criterion for percolation: if the mean interparticle separation r_{int} is shorter than r_c , the particles experience a net mutual attraction, facilitating percolation at lower particle concentrations. Approximating the mean interparticle separation as $r_{int} \sim d_p(\phi_0/\phi)^{1/2}$, the condition for percolation in the range Ca < 1 (i.e. $r_c > d_p$ or $Bo_c < 1$) becomes

Journal of Fluid Mechanics

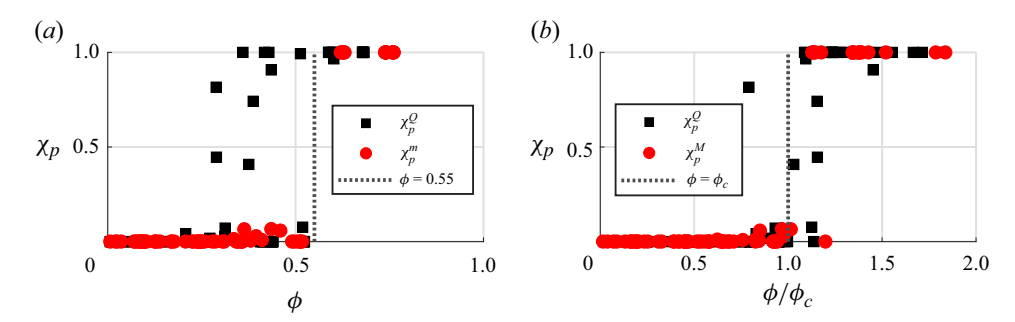


Figure 5. Percolation fraction χ_p versus (a) particle areal fraction ϕ , showing distinct percolation transitions across different experimental conditions. (b) Universal collapse of percolation data obtained by normalising ϕ by the predicted percolation threshold ϕ_c , clearly illustrating a transition at $\phi/\phi_c \approx 1$. The dashed vertical line marks the theoretical threshold, validating the unified percolation criterion.

$$r_c \geqslant d_p \left(\frac{\phi_0}{\phi}\right)^{1/2}. \tag{3.12}$$

Overall, we write the percolation criterion as

$$\phi \geqslant \phi_c = \begin{cases} \phi_0 B o_c, & B o_c < 1, \\ \phi_0, & B o_c \geqslant 1. \end{cases}$$
(3.13)

That such a criterion represents well the data is evident in figure 4(c), where (3.13) is indicated by a dashed line.

Some mismatch may be due to aspects such as nonlinearity in the drag force and modifications of the fluid flow at high concentrations. These and other aspects neglected here deserve to be investigated, though their influence on the percolation threshold does not appear to be dominant. We further confirm this threshold by plotting χ_p from all experiments as a function of the areal fraction in figure 5. While individual cases exhibit distinct percolation behaviour at different ϕ (figure 5a), plots of χ_p versus ϕ/ϕ_c display a consistent step-like transition around unity (figure 5b).

We note that the sharp transition between small and large values of χ_p reflects a distinct process with respect to general clustering. The latter, measured by χ_{cl} , is determined by a dynamic equilibrium between a multitude of breakup/aggregation events, as recently described for the present system (though at more dilute concentrations) by Qi *et al.* (2025b). In contrast, the percolation fraction concerns the existence of a system-spanning cluster: once formed, the gain/loss of particles by such an object marginally affects χ_p . This is consistent with the threshold behaviour predicted by classic percolation theory; see, e.g. Stauffer & Aharony (2018).

4. Conclusion

We have investigated clustering and percolation in dense suspensions of spheres and discs at turbulent fluid interfaces, focusing on the two most common regimes of capillary interaction: quadrupolar-dominant and monopolar-dominant.

Including discs has allowed us to test the robustness and generality of the presented framework, while extending the parameter space: particles with similarly large diameter would not be fully immersed in the thin fluid layers. Despite the fundamentally different scaling of the capillary force, a unified description emerges by defining an effective interaction length r_c at which capillary attraction and strain-induced drag are in balance.

This allows data from monopolar and quadrupolar cases to be described by a common parameter space defined solely by the interaction Bond number Bo_c and the areal fraction ϕ . The percolation transition is quantitatively predicted when the average interparticle distance $r_{int} = r_c$, leading to a simple definition of the threshold concentration. Importantly, the only parameter of such threshold, ϕ_0 , is purely geometrical and is obtained a priori by RSA calculations.

The present results unify prior observations in quadrupole-dominant systems (Shin & Coletti 2024; Shin *et al.* 2025) with the behaviour of their monopole-dominant counterparts, creating a framework valid for a broad range of interfacial turbulent suspensions. Practical applications span diverse scales and contexts, from microscopic colloids to macroscopic debris or biomaterials floating in natural bodies of water. Further extensions to other capillary interaction modes, such as dipolar forces from asymmetric particles, could further test the universality of the framework.

While capillarity has specific traits which we have attempted to unify here, the phenomenology of clustering and percolation displayed by our system can be interpreted in the broad framework of attractive particle suspensions subject to agitation. Such systems admit a jamming phase diagram in which the balance between cohesive forces and effective temperature (thermal energy or mechanical agitation) governs the transition between fluid-like and solid-like states (Trappe et al. 2001). Analogously, in the present system, the turbulent motion of the fluid may play the role of the effective temperature: at low Bo_c (or equivalently low Ca), particles rapidly form a connected network; at high Bo_c , clustering is suppressed and percolation only occurs near the geometric RSA limit in the $Bo_c-\phi$ space. However, turbulence differs fundamentally from uncorrelated thermal agitation in that it is correlated over relatively large spatio-temporal scales. Indeed, while turbulent agitation in the present system results in higher diffusivity of the particle transport, the diffusion process transitions from ballistic to diffusive around temporal scales dictated by the eddy-turnover time (Shin et al. 2025). Further investigations of how closely dense turbulent interfacial suspensions follow the canons of gas/liquid/solid phase transitions are underway.

Future research is warranted to address current limitations. First, turbulent free-surface flows with substantial depth exhibit compressible surface velocity fields not captured by the present Q2-D system (Lovecchio, Marchioli & Soldati 2013; Li et al. 2024; Qi, Li & Coletti 2025a; Qi, Xu & Coletti 2025c). Additionally, the temporal resolution of our measurements is not sufficient to discern whether clusters come to span the domain with a well-defined percolation front velocity. Identifying the latter would be important to verify whether the present system falls under the umbrella of directed percolation, which has been successfully used to interpret a wide range of phenomena including Leidenfrost effect (Chantelot & Lohse 2021), liquid-liquid demixing (Goyal, van der Schoot & Toschi 2021) and laminar-to-turbulent transition (Hof 2023). Our experiments used spherical and disc-shaped particles, leaving unexplored the impact of particle polydispersity, shape (Madivala et al. 2009; Botto et al. 2012) and electrostatic repulsion (van Baalen, Vialetto & Isa 2023), which may significantly influence clustering dynamics. Finally, comparative studies with alternative systems, such as active colloids or self-propelled particles at interfaces (Bourgoin et al. 2020; Calascibetta et al. 2024; Yang et al. 2024), could yield valuable insights into universal aggregation phenomena.

Declaration of interests. The authors report no conflict of interest.

Journal of Fluid Mechanics

REFERENCES

- ALICKE, A., STRICKER, L. & VERMANT, J. 2023 Model aggregated 2D suspensions in shear and compression: from a fluid layer to an auxetic interface? *J. Colloid Interface Sci.* 652, 317–328.
- VAN BAALEN, C., VIALETTO, J. & ISA, L. 2023 Tuning electrostatic interactions of colloidal particles at oil-water interfaces with organic salts. *Phys. Rev. Lett.* 131, 128202.
- BAKER, L.J. & COLETTI, F. 2019 Experimental study of negatively buoyant finite-size particles in a turbulent boundary layer up to dense regimes. *J. Fluid Mech.* **866**, 598–629.
- BALACHANDAR, S. & EATON, J.K. 2010 Turbulent dispersed multiphase flow. *Annu. Rev. Fluid Mech.* 42, 111–133.
- BATCHELOR, G.K. 1976 Brownian diffusion of particles with hydrodynamic interaction. *J. Fluid Mech.* **74** (1), 1–29.
- BOFFETTA, G. & ECKE, R.E. 2012 Two-dimensional turbulence. Annu. Rev. Fluid Mech. 44, 427-482.
- BOTTO, L., LEWANDOWSKI, E.P., CAVALLARO, M. & STEBE, K.J. 2012 Capillary interactions between anisotropic particles. *Soft Matter* **8** (39), 9957–9971.
- BOURGOIN, M., KERVIL, R., COTTIN-BIZONNE, C., RAYNAL, F., VOLK, R. & YBERT, C. 2020 Kolmogorovian active turbulence of a sparse assembly of interacting marangoni surfers. *Phys. Rev. X* 10 (2), 021065.
- BRANDT, L. & COLETTI, F. 2022 Particle-laden turbulence: progress and perspectives. Annu. Rev. Fluid Mech. 54, 159–189.
- Brown, E. & JAEGER, H.M. 2014 Shear thickening in concentrated suspensions: phenomenology, mechanisms and relations to jamming. *Reports Prog. Phys.* 77 (4), 046602.
- CALASCIBETTA, C., GIRALDI, L., EL KHIYATI, Z. & BEC, J. 2024 Effects of collective patterns, confinement, and fluid flow on active particle transport. *Phys. Rev. E* 110 (6), 064601.
- CHANTELOT, P. & LOHSE, D. 2021 Drop impact on superheated surfaces: short-time dynamics and transition to contact. J. Fluid Mech. 928, A36.
- Dalbe, M.-J., Cosic, D., Berhanu, M. & Kudrolli, A. 2011 Aggregation of frictional particles due to capillary attraction. *Phys. Rev. E* 83 (5), 051403.
- DENN, M.M. & MORRIS, J.F. 2014 Rheology of non-Brownian suspensions. *Annu. Rev. Chem. Biomol. Eng.* 5, 203–228.
- EVANS, J.W. 1993 Random and cooperative sequential adsorption. Rev. Mod. Phys. 65 (4), 1281.
- FULLER, G.G. & VERMANT, J. 2012 Complex fluid-fluid interfaces: rheology and structure. Annu. Rev. Chem. Biomol. Eng. 3, 519–543.
- GARBIN, V. 2019 Collapse mechanisms and extreme deformation of particle-laden interfaces. *Curr. Opin. Colloid Interface Sci.* 39, 202–211.
- GIROTTO, I., SCAGLIARINI, A., BENZI, R. & TOSCHI, F. 2024 Lagrangian statistics of concentrated emulsions. *J. Fluid Mech.* **986**, A33.
- GOYAL, A., VAN DER SCHOOT, P. & TOSCHI, F. 2021 Directional percolating pathways in demixing blends on a wetting substrate. *J. Appl. Phys.* 129 (10).
- GUAZZELLI, E., MORRIS, J.F. & PIC, S. 2011 A Physical Introduction to Suspension Dynamics. Cambridge University Press.
- HOF, B. 2023 Directed percolation and the transition to turbulence. Nat. Rev. Phys. 5 (1), 62-72.
- HOGENDOORN, W., BREUGEM, W.-P., FRANK, D., BRUSCHEWSKI, M., GRUNDMANN, S. & POELMA, C. 2023 From nearly homogeneous to core-peaking suspensions: Insight in suspension pipe flows using MRI and DNS. Phys. Rev. Fluids 8 (12), 124302.
- KIM, S. & HILGENFELDT, S. 2024 Exceptionally dense and resilient critically jammed polydisperse disk packings. Soft Matter 20 (28), 5598–5606.
- LI, Y., WANG, Y., QI, Y. & COLETTI, F. 2024 Relative dispersion in free-surface turbulence. J. Fluid Mech. 993, R2.
- LIU, I.B., SHARIFI-MOOD, N. & STEBE, K.J. 2018 Capillary assembly of colloids: interactions on planar and curved interfaces. Annu. Rev. Condens. Matter Phys. 9, 283–304.
- LOVECCHIO, S., MARCHIOLI, C. & SOLDATI, A. 2013 Time persistence of floating-particle clusters in freesurface turbulence. *Phys. Rev. E* 88 (3), 033003.
- MADIVALA, B., FRANSAER, J. & VERMANT, J. 2009 Self-assembly and rheology of ellipsoidal particles at interfaces. *Langmuir* 25 (5), 2718–2728.
- MARIN, A. & SOUZY, M. 2024 Clogging of noncohesive suspension flows. *Annu. Rev. Fluid Mech.* 57, 89–116.
- MATAS, J.-P., MORRIS, J.F. & GUAZZELLI, E. 2003 Transition to turbulence in particulate pipe flow. *Phys. Rev. Lett.* **90** (1), 014501.

S. Shin and F. Coletti

- MÖBIUS, W., TESSER, F., ALARDS, K.M.J., BENZI, R., NELSON, D.R. & TOSCHI, F. 2021 The collective effect of finite-sized inhomogeneities on the spatial spread of populations in two dimensions. *J. R. Soc. Interface.* **18** (183), 20210579.
- MONCHAUX, R., BOURGOIN, M. & CARTELLIER, A. 2012 Analyzing preferential concentration and clustering of inertial particles in turbulence. *Intl J. Multiphase Flow* 40, 1–18.
- MORRIS, J.F. 2020 Shear thickening of concentrated suspensions: recent developments and relation to other phenomena. *Annu. Rev. Fluid Mech.* **52** (1), 121–144.
- VAN DER NAALD, M., SINGH, A., EID, T.T., TANG, K., DE PABLO, J.J. & JAEGER, H.M. 2024 Minimally rigid clusters in dense suspension flow. *Nat. Phys.* 20 (4), 653–659.
- PICANO, F., BREUGEM, W.-P. & BRANDT, L. 2015 Turbulent channel flow of dense suspensions of neutrally buoyant spheres. *J. Fluid Mech.* **764**, 463–487.
- PROTIÈRE, S. 2023 Particle rafts and armored droplets. Annu. Rev. Fluid Mech. 55, 459-480.
- QI, Y., LI, Y. & COLETTI, F. 2025a Small-scale dynamics and structure of free-surface turbulence. J. Fluid Mech. 1007, A3.
- QI, Y., SHIN, S. & COLETTI, F. 2025b Breakup and coalescence of particle aggregates at the interface of turbulent liquids. *J. Fluid. Mech.* (in press).
- QI, Y., XU, Z. & COLETTI, F. 2025c Restricted Euler dynamics in free-surface turbulence. J. Fluid Mech. 1002, A38.
- SEDES, O., MAKSE, H.A., CHAKRABORTY, B. & MORRIS, J.F. 2022 K-core analysis of shear-thickening suspensions. *Phys. Rev. Fluids* 7 (2), 024304.
- SHIN, S. & COLETTI, F. 2024 Dense turbulent suspensions at a liquid interface. J. Fluid Mech. 984, R7.
- SHIN, S., COLETTI, F. & CONLIN, N. 2023 Transition to fully developed turbulence in quasi-two-dimensional electromagnetic layers. *Phys. Rev. Fluids* 8 (9), 094601.
- SHIN, S., STRICKER, L. & COLETTI, F. 2025 Particle clustering and dispersion in dense turbulent interfacial suspensions. *J. Fluid Mech.* **1013**, A31.
- SINGH, P. & JOSEPH, D.D. 2005 Fluid dynamics of floating particles. J. Fluid Mech. 530, 31-80.
- STAMOU, D., DUSCHL, C. & JOHANNSMANN, D. 2000 Long-range attraction between colloidal spheres at the air-water interface: the consequence of an irregular meniscus. *Phys. Rev. E* **62** (4), 5263–5266.
- STAUFFER, D. & AHARONY, A. 2018 Introduction to Percolation Theory. Taylor & Francis.
- TOSCHI, F. & BODENSCHATZ, E. 2009 Lagrangian properties of particles in turbulence. *Annu. Rev. Fluid Mech.* **41** (1), 375–404.
- Trappe, V., Prasad, V., Cipelletti, L., Segre, P.N. & Weitz, D.A. 2001 Jamming phase diagram for attractive particles. *Nature* **411** (6839), 772–775.
- VELLA, D. & MAHADEVAN, L. 2005 The "cheerios effect". Am. J. Phys. 73 (9), 817-825.
- VOWINCKEL, B. 2024 It takes three to tangle. J. Fluid Mech. 990, F1.
- WAGNER, N.J. & Brady, J.F. 2009 Shear thickening in colloidal dispersions. *Phys. Today* 62 (10), 27–32.
- YANG, Q., JIANG, M., PICANO, F. & ZHU, L. 2024 Shaping active matter from crystalline solids to active turbulence. *Nat. Commun.* 15 (1), 2874.